ChemComm

COMMUNICATION

View Article Online
View Journal | View Issue

Cite this: *Chem. Commun.*, 2024, 60, 7713

Received 17th May 2024,
Accepted 11th June 2024

DOI: 10.1039/d4cc02372b

rsc.li/chemcomm

Inverse kinetic isotope effect of ammonia decomposition over Ru/CeO_2 using deuterated ammonia†

Takuya Suguro, Fuminao Kishimoto,* Sota Kuramoto, William J. Movick and Kazuhiro Takanabe*

This study investigated the ammonia decomposition mechanism over Ru/CeO_2. Isotopic tests using ND_3 revealed that the rate-determining step involves adsorbed nitrogen atoms on Ru. Moreover, an inverse kinetic isotope effect where ND_3 decomposition was faster than NH_3 was clearly observed. The origin of the inverse effect was explained by the lower D coverage on the catalyst surface compared to H coverage for mitigating the inhibition of ND_3 activation.

Green hydrogen (H_2) generated using renewable energy is attracting attention as a next-generation fuel that could replace fossil fuels.[1–4] Studies have been examining the chemical conversion of H_2 into the form of a hydrogen carrier, such as ammonia (NH_3), which is easily liquefied, transported, and stored. A supply chain is envisioned in which green H_2 is produced using renewable energy, chemically converted to NH_3, and then transported to urban areas for use as fuel. When NH_3 is used as a fuel, there are two possible cases: N_2 and H_2O production by direct transformation of NH_3 and NH_3 decomposition reaction to extract pure hydrogen and then using that as a fuel. Thanks to recent research on combustion equipment development, NH_3 combustion engines with reduced NO_x emissions are being realized.[5] On the other hand, the NH_3 decomposition process leads to pure H_2, which can be widely used for conventional fuel cells or as chemical feedstocks.

NH_3 can be decomposed using various metals.[6–11] Ru shows outstanding performance for NH_3 decomposition under high NH_3 concentrations and shows optimal dissociative N_2 adsorption energy.[8–12] The various types of support materials were investigated for enhancing the NH_3 decomposition performance over the Ru catalyst, *e.g.* CeO_2[10,11] (with PrO_x[13]), $MgAl_2O_4$,[14] Al_2O_3,[15] carbon nanotubes,[16–18] carbon nanofiber,[19] SiC,[20] C12A7:e^- (ref. 21), and MgO[8,9] with various exposed crystal facets.[22]

The differences in ammonia decomposition kinetics in terms of the exposed facets of Ru[23–25] have been investigated. Egawa *et al.* demonstrated NH_3 and ND_3 isotope tests at ultra-low ammonia pressure ($\sim 10^{-5}$ kPa) over single-crystal surfaces of Ru (1110) and Ru (001), which showed the normal kinetic isotope effect (NH_3 decomposition occurred faster than ND_3 decomposition).[23] The rate-determining step was N–H bond cleavage under such low ammonia pressure conditions. Tsai *et al.* demonstrated a temperature dependence of the reaction rate of Ru (0001) and showed that the associative desorption of N_2 was the rate-determining step below 377 °C. The rate-determining step changed to cleavage of the N–H bonding at higher temperature.[24] A study using density functional theory predicted that the formation of the molecular nitrogen would be the rate-determining step with Ru (0001) and Ru (111).[25] The Temkin–Pyzhev model is widely accepted to express the ammonia decomposition kinetics and assumes that associative N_2 desorption step is the rate-determining step.[15,26] This model fits well with conditions where reaction inhibition by hydrogen is observed at low temperatures or high pressures.[27] However, several other models of reaction kinetics show different rate-determining steps.[28–30] Armenise *et al.* reported a microkinetic analysis of ammonia decomposition with a Langmuir–Hinshelwood approach and modeled the reaction to predict an integral reactor by assuming the rate-determining step to be N_2 desorption and strong hydrogen and ammonia adsorption.[31]

Although isotope experiments are a powerful tool for examining rate-determining steps, to our best knowledge, there are hardly any reports on isotope tests in the pressure range where reaction inhibition by adsorbed molecules is observed. Antunes *et al.* demonstrated the normal kinetic isotope effect over supported Ru/Al_2O_3 at an ammonia partial pressure of 1.5 Pa.[32] However, different ammonia partial pressures should result in different catalyst surface coverage and thus different kinetics.[12]

Department of Chemical System Engineering, School of Engineering, The University of Tokyo, 7-3-1 Hongo, Bunkyo-ku, Tokyo, Japan.
E-mail: kfuminao@chemsys.t.u-tokyo.ac.jp, takanabe@chemsys.t.u-tokyo.ac.jp

† Electronic supplementary information (ESI) available: Experimental methods, partial pressure dependence, and fitting result. See DOI: https://doi.org/10.1039/d4cc02372b

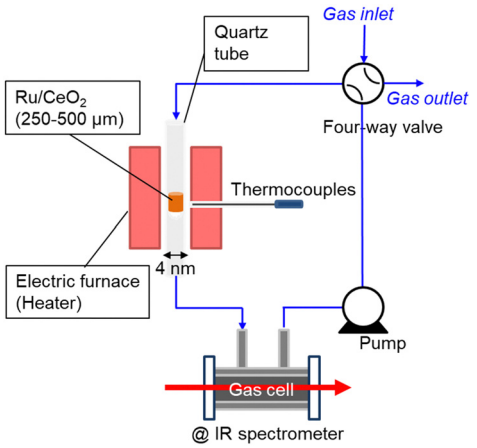

Fig. 1 Schematic diagram of the closed recirculation batch system for catalytic ammonia decomposition.

Therefore, this paper reports the kinetic isotope effect of ammonia decomposition reaction using ND_3 at 1 kPa over Ru/CeO_2 (TEM image is shown in Fig. S1, ESI†). Fig. 1 shows the experimental setup used for NH_3 decomposition. The catalyst bed was placed in a quartz tube with an internal diameter of 4 mm and heated with an electric furnace. The temperature of the cylindrical catalyst bed was measured using a thermocouple located outside the quartz tube at the catalyst bed. The catalytic reaction was performed with a closed circulation configuration (gradient-less batch reactor). The quantity of the accumulated NH_3 gas was estimated from the infrared absorption spectra passing through the in-line gas cell.

Fig. S2(a) (ESI†) shows typical results of the NH_3 decomposition at various temperatures over a supported Ru/CeO_2 catalyst. Deposition of colloidal Ru nanoparticles (mean particle size ~4 nm) on the CeO_2 support was employed to eliminate particle-size effects among the different samples. For tests at higher temperature, the Ru-deposited CeO_2 catalyst was diluted with pristine CeO_2 to control the reaction rate. As shown in Fig. S2(b) (ESI†), the NH_3 decomposition rates were obtained from the slope of the line connecting the several plotted points in Fig. S2(a) (ESI†).

Fig. 2 shows the partial pressure dependence of ammonia decomposition over the supported Ru/CeO_2 catalyst. The apparent kinetic order with respect to NH_3 partial pressure was 0.23 at 200 °C, which gradually increased with the temperature, reaching 0.62 at 400 °C. Next, N_2 was introduced into the initial gas composition to study its partial pressure dependence on the reaction rate. The N_2 partial pressure was insensitive to the NH_3 decomposition rate at both 200 and 400 °C (Fig. 2(b)).

H_2 introduction caused a decrease of the ammonia decomposition rate at 200–400 °C. Substantially negative order of −0.66 on H_2 partial pressure was observed at 200 °C (Fig. 3). The inhibition effects by H_2 became less severe with increasing temperature, reaching −0.35 at 400 °C.

Elementary reaction steps were examined for detailed analysis of the kinetics as follows:

$$NH_3 + * \overset{K_1}{\rightleftharpoons} NH_3^* \quad (1)$$

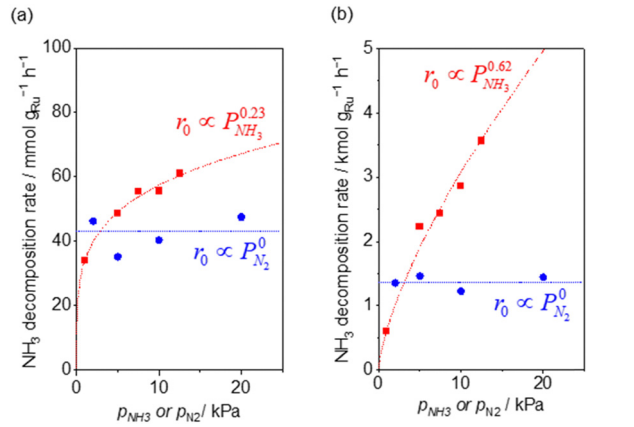

Fig. 2 NH_3 (red square) and N_2 (blue circle) pressure dependence of ammonia decomposition rates (a) over 0.1 mg of 5 wt% Ru/CeO_2 diluted with 9.9 mg of CeO_2 within pellets at 200 °C and (b) over 1 mg pellets of 10× further dilution with CeO_2 within the pellets at 400 °C. Initial conditions: ~0.5 kPa NH_3 balanced with Ar, total 101 kPa. Raw data are shown in Fig. S3 and S4 (ESI†).

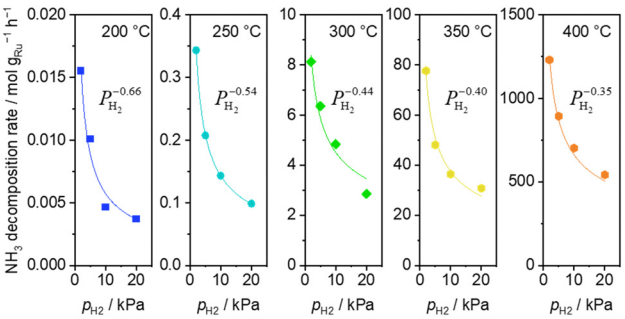

Fig. 3 H_2 pressure dependence of ammonia decomposition rates over 0.1 mg of 5 wt% Ru/CeO_2 diluted with 9.9 mg of CeO_2 within the pellets at 200 (blue square), 250 (light blue circle) and 300 °C (green diamond) and over 1 mg pellets of 10× further dilution with CeO_2 within pellets at 350 (yellow pentagon) and 400 °C (orange pentagon) (5 kPa NH_3, balanced by Ar). Raw data are shown in Fig. S5 (ESI†).

$$NH_3^* + * \overset{K_2}{\rightleftharpoons} NH_2^* + H^* \quad (2)$$

$$NH_2^* + * \overset{K_3}{\rightleftharpoons} NH^* + H^* \quad (3)$$

$$NH^* + * \overset{K_4}{\rightleftharpoons} N^* + H^* \quad (4)$$

$$2N^* \overset{K_5}{\rightleftharpoons} N_2^* \quad (5)$$

$$N_2^* \overset{K_6}{\rightleftharpoons} N_2 + * \quad (6)$$

$$H_2 + 2^* \overset{K_7}{\rightleftharpoons} 2H^* \quad (7)$$

in which * denotes active sites, and k_i and K_i represent the reaction constant and adsorption equilibrium constant of reaction i, respectively.

Fig. 4(a) shows the Arrhenius plot of NH_3 and ND_3 decomposition over the supported Ru/CeO_2 catalyst. Notably, an

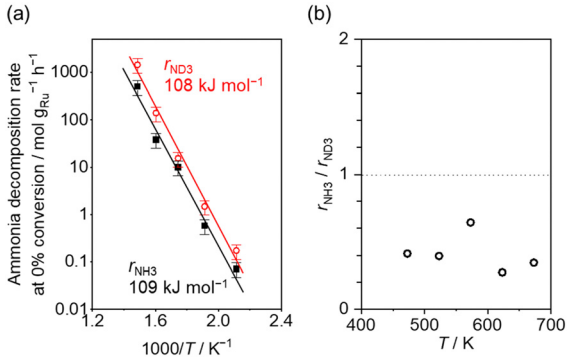

Fig. 4 (a) Arrhenius plot of NH_3 (black square) and ND_3 (red circle) decomposition over 0.1 mg of 5 wt% Ru/CeO_2 diluted with 9.9 mg of CeO_2 within pellets below 300 °C and over 1 mg pellets of 10× further dilution with CeO_2 within pellets above 400 °C. The initial gas ratio was $Ar : NH_3$ = 100 : 1 kPa or Ar/ND_3 = 100 : 1 kPa. The raw data are shown in Fig. S6–S10 (ESI†). Error bars: 34.1% (1σ of Gaussian distribution). (b) Ratio of NH_3 decomposition rate, r_{NH_3}, to ND_3 decomposition rate, r_{ND_3}, as a function of reaction temperature. Averaged r_{NH_3}/r_{ND_3} was 0.414 with a standard error of 0.062 (standard deviation = 0.139).

inverse kinetic isotope effect was observed at all temperatures, where the decomposition rate of ND_3 was greater than that of NH_3. The apparent activation energy for NH_3 and ND_3 decomposition was almost identical (109 and 108 kJ mol^{-1}). If N–H bond breaking (steps (2–4)) is involved in the rate-determining step, the activation energies should obviously be different. Therefore, the identical activation energy suggested that the rate-determining step should be steps (1), (5), (6) and (7), and most likely for associative N–N bonding formation (step (5)).

Fig. 4(b) shows the ratio of NH_3 and ND_3 decomposition rates (r_{NH_3}/r_{ND_3}) in the Arrhenius expression. The degree of kinetic isotope effect was independent of the reaction temperature and was almost constant (~0.5). Aika and Ozaki studied the inverse kinetic isotope effect on NH_3 synthesis (*i.e.*, reverse reaction of NH_3 decomposition). Strong inverse kinetic isotope effects were observed in the reaction of H_2 and D_2 with N_2 over iron,[33,34] molybdenum-based,[35] or even Ru-based[36,37] catalysts. The inverse kinetic isotope effects were explained by the larger equilibrium constant for ND_3 decomposition relative to NH_3 decomposition, which increased the empty sites for N_2 activation.

Based on elementary steps (1)–(7), the overall reaction rate can be expressed as follows with an assumption of nitrogen triple bond formation in step (5) as the rate-determining step (adopted from Stoltze[38]).

$$-r_{NH_3} = r_5 = k_5^+ K_1^2 K_2^2 K_3^2 K_4^2 K_7^{-3} \left({P_{NH_3}}^2 {P_{H_2}}^{-3} - \frac{P_{N_2}}{K_g} \right) {\theta_*}^2 \quad (8)$$

$$\theta_* = \left[1 + \left(\frac{P_{N_2}}{K_6} \right)_{N_2} + \left(\frac{K_1 K_2 K_3 K_4 P_{NH_3}}{K_7^{1.5} {P_{H_2}}^{1.5}} \right)_{N} + \left(\frac{K_1 K_2 K_3 P_{NH_3}}{K_7 P_{H_2}} \right)_{NH} + \left(\frac{K_1 K_2 P_{NH_3}}{K_7^{0.5} {P_{H_2}}^{0.5}} \right)_{NH_2} + \left(K_1 P_{NH_3} \right)_{NH_3} + \left(K_7^{0.5} {P_{H_2}}^{0.5} \right)_{H} \right]^{-1} \quad (9)$$

K_g and θ_* represent the equilibrium constant of the overall ammonia decomposition reaction at given conditions and the fraction of empty sites, respectively. The first assumption is that H is the most abundant reactive intermediate (MARI) because of the negative partial pressure dependence on H_2. However, if the terms other than hydrogen are eliminated from eqn (9), the partial pressure dependence of the reaction rate on hydrogen becomes negative fourth order, which is too large compared to the experimental results.

$$-r_{NH_3} = \frac{k_5^+ K_1^2 K_2^2 K_3^2 K_4^2 {P_{NH_3}}^2}{K_7^2 {P_{H_2}}^4} \quad (10)$$

Assuming NH_3 as the MARI, the order of the partial pressure dependence on H_2 is still minus three. To be consistent with the zero order of N_2 and the slightly negative order of H_2 demonstrated by experiments, we derived the rate expression by assuming NH or NH_2 species as the MARI, respectively:

$$-r_{NH_3} = \frac{k_5^+ K_4^2}{K_7 P_{H_2}} \quad (11)$$

or

$$-r_{NH_3} = \frac{k_5^+ K_3^2 K_4^2}{K_7^2 {P_{H_2}}^2} \quad (12)$$

However, none of these partial pressure dependencies fully match the experimental results (NH_3 order: 0.23 to 0.62, H_2 order: −0.66 to −0.35, N_2 order: ~0), suggesting that the balance of these adsorbed species on the surface affects the reaction rate.

From the experimental results, both the ammonia and hydrogen orders increased with increasing temperature. Typically, the surface reaction intermediates decreased as the temperature increases, meaning that the coverage term, θ_*, becomes closer to zero at higher temperatures. Therefore, based on eqn (8), the dependence on ammonia partial pressure increases with increasing temperature under ammonia partial pressure. On the other hand, the effect of reaction inhibition by intentionally introduced hydrogen weakened as the temperature increased. This change can be explained by the change in MARI with increasing temperature. At high temperatures, MARI approaches N, and the apparent hydrogen partial pressure dependence is expected to approach zero, as shown in the equation below.

$$-r_{NH_3} = k_5^+ \quad (13)$$

From the rate expression as eqn (11) or (12), one possibility for explanation of the inverse kinetic isotope effect is the difference of the equilibrium constant of H_2 or D_2 adsorption/desorption (K_7). Kellner and Bell studied H_2/D_2 isotope effects on Fischer–Tropsch synthesis over supported Ru catalysts.[39] They calculated the equilibrium constant of H_2 and D_2 adsorption on Ru from vibrational frequencies for molecular and atomically adsorbed H_2 and D_2 (derivation is shown in the ESI†). The ratio of the equilibrium constants of D_2 adsorption and that of H_2 adsorption ($K_{7,D}/K_{7,H}$) was less than 1

between 180 °C and 270 °C, or the equilibrium shifted more toward desorption for D_2 than for H_2. Based on rate expression (11) or (12), lower K_7 leads to a higher overall reaction rate due to more active surface species for the forward reaction (less inhibition). Therefore, the difference in the adsorption equilibrium constants of H_2 and D_2 can be one possible explanation for the inverse kinetic isotope effect in the NH_3 decomposition reaction over the Ru/CeO_2 catalyst observed in this study, suggesting that the secondary kinetic isotope effect appears inversely.

In conclusion, kinetic analysis using Ru/CeO_2 revealed that comparable apparent activation energies between NH_3 and ND_3 decomposition reactions ($\sim$108 kJ mol^{-1}) were obtained with an inverse kinetic isotope effect ($r_{NH_3}/r_{ND_3} \sim 0.5$). The kinetic orders were zero with respect to N_2 partial pressure and negative with respect to H_2 partial pressure on the NH_3 decomposition rate. The results suggest that the rate-determining step does not involve N–H or N–D-bond dissociation, but it likely involves N–N triple bond formation, of which the rate is strongly perturbed by the surface H(D) adsorption equilibrium from H_2 and D_2 to the Ru surface. The adsorption equilibrium constant for D_2 is smaller than that for H_2, resulting in lower D coverage than H coverage, which is advantageous for high N* coverage. It can be concluded that the observed isotope effect was the secondary kinetic isotope effect inversely influenced by H(D) surface coverage. A more comprehensive understanding of the kinetics can be attained with further studies on isotope effects under diverse conditions.

This work was financially supported by the Mohammed bin Salman Center for Future Science and Technology for Saudi-Japan Vision 2030 at The University of Tokyo (MbSC2030), and the Science and Technology Research Partnership for Sustainable Development (SATREPS) in collaboration between the Japan Science and Technology Agency (JST, JPMJSA2104) and Japan International Cooperation Agency (JICA).

Data availability

The data supporting this article have been included as part of the ESI.† Raw data for each experiment is available by contacting the corresponding author.

Conflicts of interest

There are no conflicts to declare.

Notes and references

1 A. Klerke, C. H. Christensen, J. K. Nørskov and T. Vegge, *J. Mater. Chem.*, 2008, **18**, 2304–2310.
2 S. Mukherjee, S. V. Devaguptapu, A. Sviripa, C. R. F. Lund and G. Wu, *Appl. Catal., B*, 2018, **226**, 162–181.
3 K. E. Lamb, M. D. Dolan and D. F. Kennedy, *Int. J. Hydrogen Energy*, 2019, **44**, 3580–3593.
4 N. Morlanés, S. P. Katikaneni, S. N. Paglieri, A. Harale, B. Solami, S. M. Sarathy and J. Gascon, *Chem. Eng. J.*, 2021, **408**, 127310.
5 J. S. Cardoso, V. Silva, R. C. Rocha, M. J. Hall, M. Costa and D. Eusébio, *J. Cleaner Prod.*, 2021, **296**, 126562.
6 S. Brunauer, K. S. Love and R. G. Keenan, *J. Am. Chem. Soc.*, 1942, **64**, 751–758.
7 J. C. Ganley, F. S. Thomas, E. G. Seebauer and R. I. Masel, *Catal. Lett.*, 2004, **96**, 117–122.
8 C. Chen, K. Wu, H. Ren, C. Zhou, Y. Luo, L. Lin, C. Au and L. Jiang, *Energy Fuels*, 2021, **35**, 11693–11706.
9 T. Su, B. Guan, J. Zhou, C. Zheng, J. Guo, J. Chen, Y. Zhang, Y. Yuan, W. Xie, N. Zhou, H. Dang, B. Xu and Z. Huang, *Energy Fuels*, 2023, **37**, 8099–8127.
10 I. Lucentini, A. Casanovas and J. Llorca, *Int. J. Hydrogen Energy*, 2019, **44**, 12693–12707.
11 I. Lucentini, G. García Colli, C. D. Luzi, I. Serrano, O. M. Martínez and J. Llorca, *Appl. Catal., B*, 2021, **286**, 119896.
12 A. Boisen, S. Dahl, J. K. Nørskov and C. H. Christensen, *J. Catal.*, 2005, **230**, 309–312.
13 K. Yamazaki, M. Matsumoto, M. Ishikawa and A. Sato, *Appl. Catal., B*, 2023, **325**, 122352.
14 D. Szmigiel, W. Raróg-Pilecka, E. Miśkiewicz, Z. Kaszkur and Z. Kowalczyk, *Appl. Catal., A*, 2004, **264**, 59–63.
15 W. Zheng, J. Zhang, H. Xu and W. Li, *Catal. Lett.*, 2007, **119**, 311–318.
16 S. F. Yin, B. Q. Xu, W. X. Zhu, C. F. Ng, X. P. Zhou and C. T. Au, *Catal. Today*, 2004, **93**, 27–38.
17 S. F. Yin, Q.-H. Zhang, B.-Q. Xu, W.-X. Zhu, C.-F. Ng and C.-T. Au, *J. Catal.*, 2004, **224**, 384–396.
18 S. F. Yin, B. Q. Xu, S. J. Wang, C. F. Ng and C. T. Au, *Catal. Lett.*, 2004, **96**, 113–116.
19 S. Armenise, L. Roldán, Y. Marco, A. Monzón and E. García-Bordejé, *J. Phys. Chem. C*, 2012, **116**, 26385–26395.
20 M. Pinzón, A. Romero, A. de Lucas Consuegra, A. R. de la Osa and P. Sánchez, *J. Ind. Eng. Chem.*, 2021, **94**, 326–335.
21 F. Hayashi, Y. Toda, Y. Kanie, M. Kitano, Y. Inoue, T. Yokoyama, M. Hara and H. Hosono, *Chem. Sci.*, 2013, **4**, 3124–3130.
22 H. Fang, S. Wu, T. Ayvali, J. Zheng, J. Fellowes, P.-L. Ho, K. C. Leung, A. Large, G. Held, R. Kato, K. Suenaga, Y. I. A. Reyes, H. V. Thang, H.-Y. T. Chen and S. C. E. Tsang, *Nat. Commun.*, 2023, **14**, 647.
23 C. Egawa, T. Nishida, S. Naito and K. Tamaru, *J. Chem. Soc.*, 1984, **80**, 1595.
24 W. Tsai and W. H. Weinberg, *J. Phys. Chem.*, 1987, **91**, 5302–5307.
25 X. Lu, J. Zhang, W.-K. Chen and A. Roldan, *Nanoscale Adv.*, 2021, **3**, 1624–1632.
26 S. Sun, Q. Jiang, D. Zhao, T. Cao, H. Sha, C. Zhang, H. Song and Z. Da, *Renewable Sustainable Energy Rev.*, 2022, **169**, 112918.
27 A. S. Chellappa, C. M. Fischer and W. J. Thomson, *Appl. Catal., A*, 2002, **227**, 231–240.
28 W. Pyrz, R. Vijay, J. Binz, J. Lauterbach and D. J. Buttrey, *Top. Catal.*, 2008, **50**, 180–191.
29 S. Sayas, N. Morlanés, S. P. Katikaneni, A. Harale, B. Solami and J. Gascon, *Catal. Sci. Technol.*, 2020, **10**, 5027–5035.
30 S. R. Kulkarni, N. Realpe, A. Yerrayya, V. K. Velisoju, S. Sayas, N. Morlanes, J. Cerillo, S. P. Katikaneni, S. N. Paglieri, B. Solami, J. Gascon and P. Castaño, *Catal. Sci. Technol.*, 2023, **13**, 2026–2037.
31 S. Armenise, E. García-Bordejé, J. L. Valverde, E. Romeo and A. Monzón, *Phys. Chem. Chem. Phys.*, 2013, **15**, 12104–12117.
32 R. Antunes, R. Steiner, L. Marot and E. Meyer, *Int. J. Hydrogen Energy*, 2022, **47**, 14130–14140.
33 K. Aika and A. Ozaki, *J. Catal.*, 1969, **13**, 232–237.
34 K. Aika and A. Ozaki, *J. Catal.*, 1970, **19**, 350–352.
35 K. Aika and A. Ozaki, *J. Catal.*, 1969, **14**, 311–321.
36 Y. Izumi and K. Aika, *J. Phys. Chem.*, 1995, **99**, 10346–10353.
37 Y. Izumi, Y. Iwata and K. Aika, *J. Phys. Chem.*, 1996, **100**, 9421–9428.
38 P. Stoltze, *J. Catal.*, 1988, **110**, 1–10.
39 C. S. Kellner and A. T. Bell, *J. Catal.*, 1981, **67**, 175–185.

